Carbon Neutralization

WILEY

Carbon Neutralization

RESEARCH ARTICLE OPEN ACCESS

Light Trapping Regulation of Tilted InGaN Nanowire Arrays to Enhance Photoelectrochemical Performance

Hedong Chen[1] | Mei Hu[1] | Yizhi Liao[1] | Fan Xu[1] | Dao Wang[2] | Feng Weiwei[3] | Qiu Yecheng[4] | Yin Feng[1] | Fuming Chen[1] | Wenhao Liang[4] | Guofu Zhou[5]

[1]Guangdong Engineering Technology Research Center of Efficient Green Energy and Environment Protection Materials, School of Electronic Science and Engineering (School of Microelectronics), South China Normal University, Foshan, China | [2]College of Science, Qiongtai Normal University, Haikou, China | [3]School of Resources and Environment, Nanchang University, Nanchang, Jiangxi, China | [4]Department of Applied Biology and Chemical Technology, Research Institute for Smart Energy, The Hong Kong Polytechnic University, Kowloon, Hong Kong SAR, China | [5]Guangdong Provincial Key Laboratory of Optical Information Materials and Technology, South China Academy of Advanced Optoelectronics, South China Normal University, Guangzhou, China

Correspondence: Hedong Chen (hedong.chen@m.scnu.edu.cn) | Wenhao Liang (wenhao.liang@polyu.edu.hk) | Guofu Zhou (guofu.zhou@m.scnu.edu.cn)

Received: 19 August 2025 | **Revised:** 15 September 2025 | **Accepted:** 25 September 2025

Funding: This study was supported by the National Natural Science Foundation of China (12404049), the Guangdong Basic and Applied Basic Research Foundation (2023A1515110521, 2024A1515011260), and the Start-up Fund for RAPs under the Strategic Hiring Scheme (P0058663) at The Hong Kong Polytechnic University.

Keywords: antireflection structure | InGaN nanowire arrays | light absorption regulation | molecular beam epitaxy | photoelectrochemical

ABSTRACT

The construction of efficient light-harvesting/conversion materials is the key to photoelectrochemical (PEC) water splitting. It should not be overlooked that the precise construction of materials and electrode structures plays a crucial role in the performance of its photoelectricity. Traditional structures (including dense film, pyramid and vertical nanowire (NW)) usually result in nonnegligible light loss, hierarchical antireflection structures of NW arrays on nonplanar substrates are efficient approaches to maximize the light absorption for PEC water splitting. Here, we constructed InGaN NW arrays with adjustable tilt angle on nonplanar substrates by plasma assisted-molecular beam epitaxy, and find the photoelectrical properties are closely related to their tilt angle and NW spacing. As a function of tilt, the photocurrent is dependent on the inclination, showing a trend of first increasing and then decreasing. NW arrays with more separated NWs exhibit larger photocurrent enhancement at larger tilt angle up to 116% at 81.9°. This study compiles the effects of various NW array morphologies on the PEC performance under varied light incidence angle, provides reference for the design of vertical NW arrays on nonplanar substrates acting as hierarchical antireflection structures for efficient light absorption on PEC and photoelectric applications.

1 | Introduction

Energy and environment concerns are in the focus and require urgent solutions [1–4]. Solar energy as renewable source needs to be well utilized and converted to other energy forms which can be used directly [5, 6]. Photoelectrocatalysts (PEC) water splitting for hydrogen evolution is considered a promising, environmentally friendly, and sustainable energy strategy [7–9]. However, the inevitable light reflection from the surface of solid photoelectrocatalysts leads to losses of solar light [10]. Therefore, to maximize the solar light absorption through the design of artificial antireflection structures is an efficient approach to enhance the PEC efficiency.

Recently, to achieve solar light absorption and high-performance PEC applications, various solar light harvesting nanostructures of

commonly adopted semiconductors including modified films, hollow structures, pyramids, vertical nanowire (NWs) arrays, nanocone arrays and porous structures, have been developed and investigated [11, 12]. For instance, hierarchically porous particles and heterogeneous hollow, multi-shelled structures with porous shells were prepared to harvest solar light sequentially and enhance the PEC efficiency [13]. Light trapping thin film modifications, such as the incorporation of Pd nanostructures into CuO forming a CuO:Pd light trapping thin film, were applied to enhance light absorption and PEC pollutant degradation efficiency [14]. GaN with a bimodal meso/macropore structure was fabricated to enhance the light absorption and PEC performance [15]. Porous GaN [16] with vertical holes and GaAs [17] with subwavelength texture were prepared by etching processes to reduce the light reflectance and enhance hydrogen evolution. Si NW arrays decorated with Pt nanoparticles were used to improve the PEC hydrogen generation through the light-trapping effects of the NWs [18]. Several pyramid textured Si photoelectrodes with antireflection effects have been reported [19–22]. A series of hierarchical architectures to harvest solar light for enhanced PEC properties have been realized, such as polydisperse nanoparticles, hyperbranched column-like structures, nanobowl, hollow nanospheres enabling multiple intra-cavity reflections, metal substructures integrated into hierarchical architectures, gradient refractive index nanostructures, discontinuous patterns for antireflection, and more [23, 24].

For NW semiconductors, they have been widely investigated as photoelectrodes for PEC and photoelectric fileds due to enahnced light trapping effect and high specific surface area [25–29]. For instance, $In_xGa_{1-x}N$ and $Ga_xAs_{1-x}P$ nanowires/nanorods vertically grown on planar Si substrates have been used for light absorption- and PEC reaction enhancement [30–33]. To further improve the light trapping, researchers found that tilt NW structure could dramatically boost the light absorption. ZnO nanorods, vertically aligned on a polyethylene terephthalate flexible substrate were bended to improve the light trapping and the PEC efficiency [34]. Furthermore, multi-band InGaN NW arrays on a nonplanar Si wafer with tilt angles of 52° [35] and 31° [36] were fabricated for light absorption and PEC water splitting improvement. Unfortunately, these publised studies lack of optimization and maxmization of light trapping and PEC efficiency. Besides, it has been discovered that the tilt of GaAsP NWs vertically aligned on a planar Si substrate revealed a maximum enhancement of the photocurrent density for PEC water splitting for a tilt angle of 60° from the light incidence direction. The optimization of the photocurrent density for controlled NW morphology and spacing was speculated [37]. Furthermore, in our previous work, we found that InGaN NWs with a tilt angles of 73° delivered the maximized photocurrent density, which was different from the tilt angle (60°) of above reference. Therefore, the light trapping effect is not only related to tilt angle, but also dependent on the NW spacing.

Here, we experimentally study the dependence of the PEC performance for solar water splitting on the tilt of InGaN NW arrays with various dispersion density, fabricated by plasma assisted-molecular beam epitaxy (PA-MBE). For vertical light incidence, the NW array with suitable-density, well-separated NWs exhibits the highest photocurrent due to enhanced light absorption in combination with the large surface area. For all NW arrays, the photocurrent reveals a distinct maximum when the light incidence is tilted away from the surface normal. NW arrays with larger NW spacing exhibit the largest photocurrent enhancement of up to 116% at a light incident angle of 81.9°. In addition, numerical finite difference time domain (FDTD) simulations demonstrate bigger tilt nanowires exhibit enhanced minimum light reflectivity. This provides a guide for the design and realization of more complex NW arrays on nonplanar substrates to form efficient, hierarchical antireflection structures for maximized light ultilization in optical devices.

2 | Experimental Section

2.1 | Growth of Various InGaN NW Arrays on Planar Si (111) Substrates

Before growth, the Si wafers were first immersed in 10 wt.% HF aqueous solution to remove the native oxide layer. Then, the clean Si wafers were loaded into the MBE chamber for degassing, nitridation, and InGaN growth. The detailed growth process can be found in our previous work [38]. The SiN_x layer formed by surface nitridation before InGaN growth accommodates the lattice mismatch and reduces the threading dislocation density, improving the crystal quality of InGaN [39, 40] without reducing the conductivity for moderate nitridation times [4]. The molecular N_2 gas flow rate for the plasma source was 1.7 sccm (standard cubic centimeter per minute).

2.2 | Materials Characterization

The In contents of the various InGaN NW arrays were determined by X-ray diffraction (XRD, PANalytical X'Pert PRO). The surface morphologies and cross-sections were measured by Field-emission scanning electron microscopy (FE-SEM; ZEISS Gemini 500) and atomic force microscopy (AFM; Bruker Multimode 8). The detailed InGaN NW structure was characterized by transmission electron microscopy (TEM; JEM-2100HR). The reflectivity of all samples was measured by an optical spectrometer (Ocean Maya2000PRO). Here, we used FDTD simulations with a commercial code (Lumerical Inc.) to calculate the reflected electric field distribution. The detailed parameters can be seen in our previous work [35, 41]. In addition, the tilt angles of InGaN nanowire samples were 0°, 50°, and 73°. The wavelength of the vertical, linear polarized incident light beam was 550 nm.

2.3 | Photoelectrochemical Measurements

The preparation of the InGaN photoanodes was described in our previous work [41]. Linear sweep voltammetry (LSV) curves under chopped on-off light were taken with a scan rate of 50 mV s^{-1} from −0.3 to 0.4 V versus Ag/AgCl. The power density of the simulated sun light was 100 mW cm^{-2} (GLORIA-X500A). Electrochemical impedance spectroscopy (EIS) measurements were performed in the frequency range from 1 Hz to 100 kHz at 0.3 V in 0.5 M (mol L^{-1}) Na_2SO_4. Mott–Schottky (M-S) plots of capacitance-voltage (C-V) measurements were acquired in the dark in the potential range from −0.8 to 0.6 V versus Ag/AgCl in 0.5 M Na_2SO_4.

3 | Result and Discussion

The InGaN samples used for photoelectrochemical devices were fabricated by growing InGaN with various NW spacings, lengths and shapes on planar n-type Si (111) wafers with a 0.0001–0.0009 Ωcm resistivity via PA-MBE [38]. The detailed growth process can be found in experimental section of supporting materials. Schemes of the MBE system and growth process of the InGaN NW arrays with various morphologies, denoted InGaN-1–4, are shown in Figure 1a,b. Supporting Information: Figure S1 in the supporting materials presents diagrams of the growth conditions, that is, substrate temperature (thermocouple reading), In and Ga beam equivalent pressures, In and Ga shutter sequences and forward power of the active N plasma source versus the growth time for InGaN-1–4. The PEC properties of the InGaN photoanodes were measured in an aqueous solution of 0.5 M Na_2SO_4 with 0.5 M Na_2SO_3 using an electrochemical workstation in three-electrode configuration, with the InGaN-1–4 working electrodes, an Ag/AgCl reference electrode and a Pt mesh counter electrode. All detailed experimental process can be seen in supporting materials.

The XRD spectra recorded around the Si (111) Bragg reflection for the InGaN-1–4 NW arrays are plotted in Supporting Information: Figure S2. The peaks at 28.44° are from the Si (111) substrates. The peaks for the InGaN-1–4 NW arrays, due to the InGaN (0002) Bragg reflection, are all centered around 34.18°. The In content is calculated according to Bragg's law, $2d \cdot \sin\theta = n \cdot \lambda$ $(n = 1)$ and Vegard's law, $d_{InGaN} = x \cdot d_{InN} + (1-x) \cdot d_{GaN}$ [35]. d is the InGaN lattice constant, $2\theta_{InN}$ is 31.34° and $2\theta_{GaN}$ is 34.56°. This gives the In (Indium) content of 11%, corresponding to a bandgap energy of 2.96 eV, which is calculated from $E_g(InGaN) = x \cdot E_g(InN) + (1-x) \cdot E_g(GaN) - b \cdot x \cdot (1-x)$, with $E_g(InN) = 0.7$ eV and $E_g(GaN) = 3.4$ eV [42, 43], assuming a bowing parameter b of 1.5. To analyze the structural characterization, TEM and high-resolution TEM images of individual InGaN-3 NWs are displayed in Supporting Information: Figure S3a,b. The diameter of the InGaN NW is around 70 nm in Supporting Information: Figure S3a. From the high-resolution TEM image in Figure S3b, regular lattice fringes perpendicular to the NW sidewall are observed, indicating the single-crystal structure and the NW growth direction along the c-axis.

The morphologies of the InGaN-1–4 NW arrays vary from fully coalesced NWs to isolated, well-separated NWs, depending on the adjustment of the growth conditions, mainly the Si substrate temperature, the ratio of the In and Ga beam equivalent pressures and the N plasma source power, summarized in Supporting Information: Figure S1. The top-view- and cross-sectional field-emission scanning electron microscopy (SEM) images of the InGaN-1–4 NW arrays are shown in Figure 2a–d. Figure 2a of the InGaN-1 NW array reveals coalesced NWs. Tiny gaps and directional fluctuations of the coalescence of the NWs are observed. The NWs are connected from the bottom to the top with relatively straight sidewalls. After increasing the power of the N plasma source from 350 to 500 W and the In and Ga beam equivalent pressures from 0.42×10^{-7} and 0.69×10^{-7} Torr to 0.53×10^{-7} and 1.39×10^{-7} Torr, respectively, the degree of NW coalescence is reduced with the NWs only connected in one direction, forming nanowalls for the InGaN-2 NW array, as presented in Figure 2b. There are nanogaps of 10–80 nm width between the InGaN nanowalls, as seen in the top-view SEM image. However, the cross-sectional SEM image of the InGaN-2 NW array in Figure 2c reveals still rather compact NWs, at least

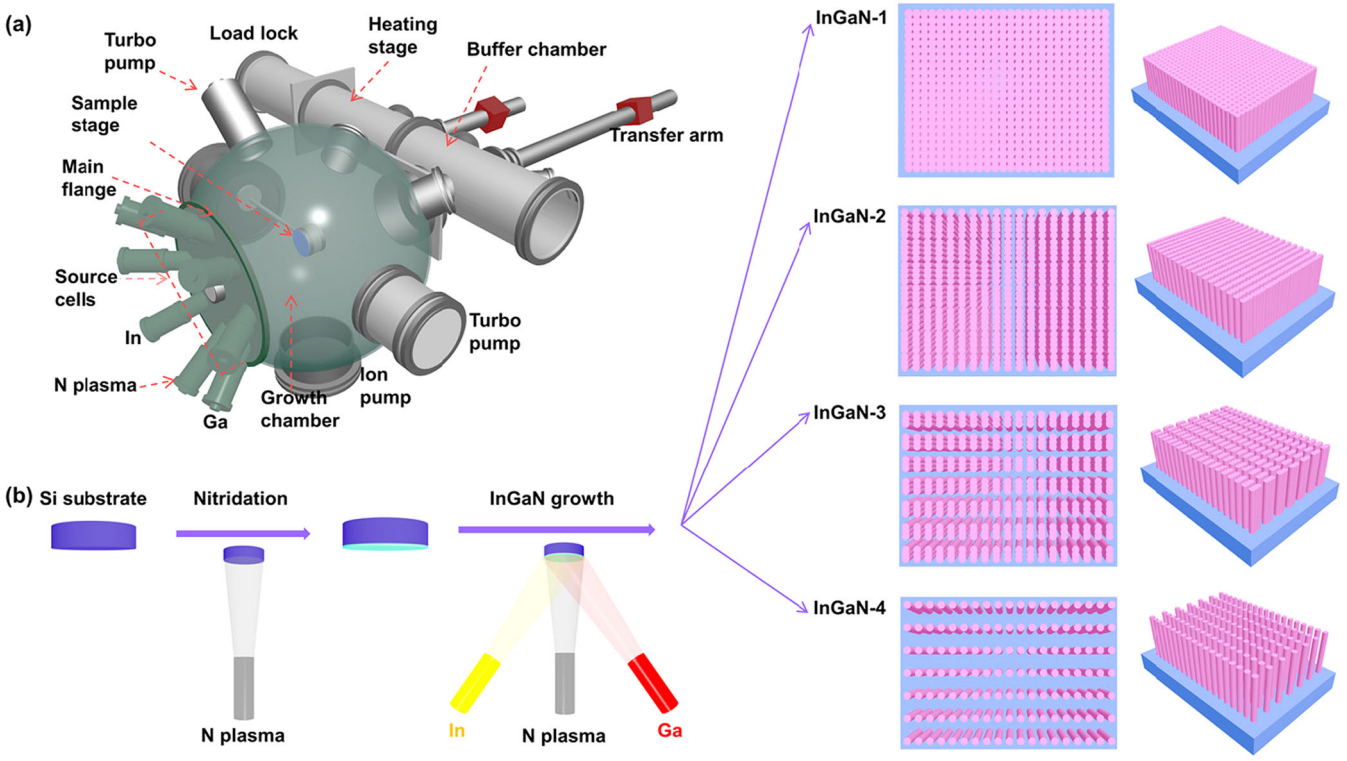

FIGURE 1 | Schematic diagrams of (a) molecular beam epitaxy (MBE) system and (b) growth process of InGaN-1–4 nanowire (NW) arrays with various morphologies.

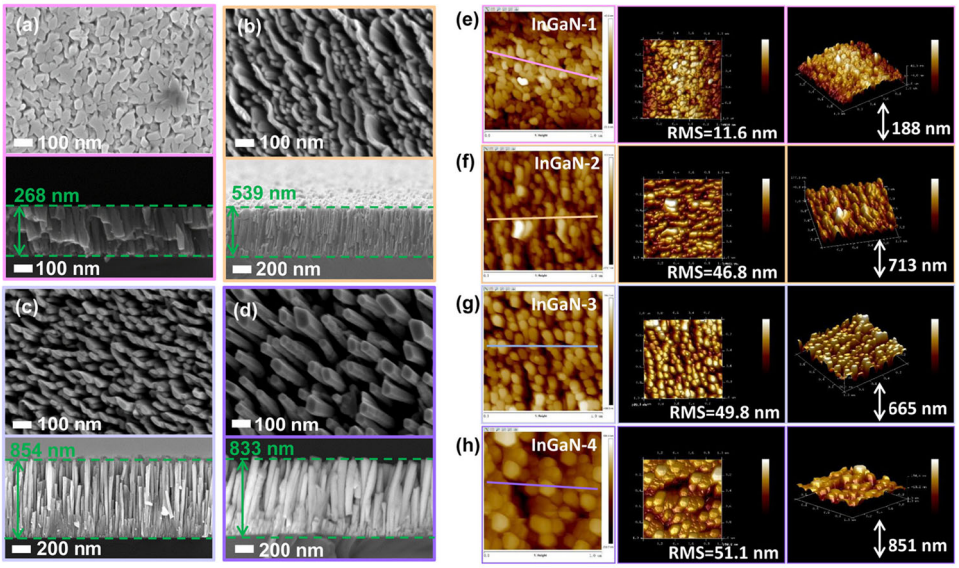

FIGURE 2 | Top-view atomic force microscopy (AFM) height images and three-dimensional (3D) images, and top-view- and cross-sectional scanning electron microscopy (SEM) images of InGaN samples. (a–d) and (e–h) correspond to InGaN-1, InGaN-2, InGaN-3, and InGaN-4, respectively.

in one direction. When the power of the N plasma source is reduced back to 350 W and the substrate temperature is ramped up to 700°C, the NWs of InGaN-3 NW array become more isolated with only a few NWs connected in one direction. This is also reflected in the cross-sectional SEM image. For the InGaN-4 NW array, where the Ga beam equivalent pressure is decreased from 1.39×10^{-7} to 1.03×10^{-7} Torr and the In beam equivalent pressure is increased from 0.53×10^{-7} to 0.72×10^{-7} Torr, the gaps between the NWs are larger, 80–150 nm, with NW diameters of 40–80 nm, as observed in Figure 2d. As seen in both, the top-view- and cross-sectional SEM images, the NWs are now isolated, well-separated. The vertical and lateral growth rates for the InGaN-1–4 NW arrays can be estimated from the lengths of the NWs. InGaN-3 and InGaN-4 exhibit longer NWs (854 nm and 833 nm) than InGaN-1 and InGaN-2, indicating that they possess higher axial NW growth rates, leading to the observed more separated NWs.

To further evaluate the morphology of the InGaN NW arrays, the surface morphologies and cross-sections were measured by atomic force microscopy (AFM) and field-emission scanning electron microscopy (FE-SEM). 3D images and AFM height- of InGaN-1–4 are shown in Figure 2e–h. The height images of InGaN-1–3 in Figure 2e–g reveal similar sized NWs. The degree of coalescence of the NWs for InGaN-2–4 in Figure 2f–h decreases compared to that for InGaN-1 with fully coalesced NWs. For InGaN-2 in Figure 2f the InGaN nanowalls are confirmed, which break up into more isolated, dense NWs for InGaN-3 in Figure 2g. Finally, the NWs become isolated, well-separated with larger diameter and spacing for InGaN-4, shown in Figure 2h. These results are consistent with those from the SEM images in Figure 2a–d. Furthermore, the root mean square (RMS) [43] roughness values obtained from the AFM analysis can be used to indicate the diameter-to-spacing relation of the NWs. As presented in Table 1, InGaN-1–4 exhibit RMS roughness values of 11.6, 46.8, 49.8, and 51.1 nm, respectively, which are obtained from the AFM measurements in Figure 2e–h. As for the RMS roughness, the measured height variation for high-aspect ratio, separated NWs is geometrically given by the AFM tip angle and NW spacing. Additionally, the corresponding height profiles along the solid lines in top-view AFM height images of four InGaN samples are presented in Supporting Information: Figure S4. InGaN-1 shows slight height fluctuations and tiny gaps, indicating a relatively flat surface. Differently, InGaN-2–4 display height variations that increase in magnitude, reflecting the increase of the NW spacing. The average height variations increase only slightly for InGaN-2 to InGaN-3 while there is a drastic increase for InGaN-4 due to the isolated, well-separated NWs with larger diameter and spacing.

TABLE 1 | RMS roughness values for InGaN-1, InGaN-2, InGaN-3, and InGaN-4 obtained from AFM measurements in Figure 2e–h.

Samples	InGaN-1	InGaN-2	InGaN-3	InGaN-4
RMS (nm)	11.6	46.8	49.8	51.1

Abbreviations: AFM, atomic force microscopy; RMS, root mean square.

To elucidate the effects of the morphology on the light adsorption and PEC water splitting performance, the average height variations correlate with the light reflectivity under normal light incidence for InGaN-1–4 in Figure 3a and the LSV curves of InGaN-1–4 in the potential range from −0.3 to 0.4 V versus Ag/AgCl under on/off chopped light are presented in Figure 3b. The reflectivity is largest for InGaN-1 and continuously decreases with the smallest reflectivity for InGaN-4. The main reason is that light scattering and absorption increase for NW arrays with isolated, well-separated NWs with larger spacing, coming closer to the light wavelength. The InGaN-1 photoanode with a relatively flat surface displays the lowest photocurrent density of about 0.03 mA cm^{-2} at 0.3 V versus Ag/AgCl. For the InGaN-2 nanowall photoanode, the photocurrent density is increased by up to 0.02 mA cm^{-2}. The InGaN-3 and InGaN-4 NW photoanodes exhibit the largest photocurrent densities at the same bias of 0.067 and 0.064 mA cm^{-2}, respectively. The enhancement of the photocurrent density correlates

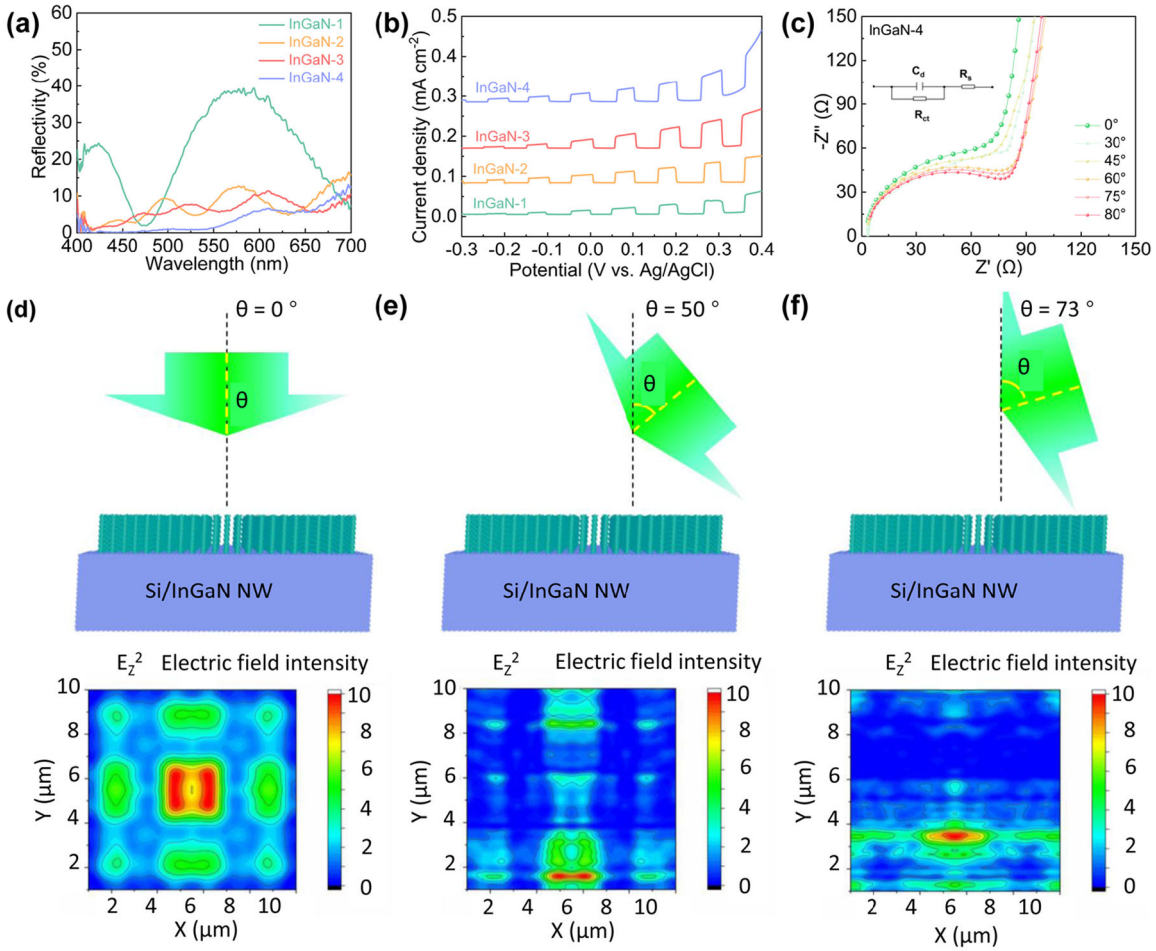

FIGURE 3 | (a) Reflectivity spectra of InGaN-1–4 for normal light incidence. (b) Current density - voltage of InGaN-1, InGaN-2, InGaN-3, and InGaN-4 photoanodes under on/off chopped light. (c) Nyquist plots of the EIS measurements for InGaN-4 photoanode for varied angles of incident light. Schematic diagrams and two-dimensional (2D) color coded reflected electric field distributions for the Si/InGaN NWs as a function of the tilt angle of the incident light, (d) 0°, (e) 50°, and (f) 73°. The incident linear polarized light wavelength is 550 nm. The reflected intensity ratios are 1/0.63/0.39.

well with the light trapping properties for InGaN-1–3, while the photocurrent density for InGaN-4 is slightly smaller than that for InGaN-3. This means that the delicate balance between absorption, photocarrier separation and transfer, surface reaction rate and surface area have to be taken into account to understand the photocurrent density. First of all, InGaN-1–4 have the same In content, and therefore, the same bandgap energy and absorption coefficient. Also the surface reaction rate, then, can be assumed to be similar. Hence, the antireflection properties dominate for InGaN-1–3 while carrier separation and transport and surface area become more important for the thicker and more sparse NWs of InGaN-4. We will address this more deeply by the EIS- and C-V measurements shown below. To note, the absence of any contribution of the Si substrate to the PEC measurements, especially for the well-separated NWs and the high long-time chemical stability of InGaN NWs has been deeply investigated and confirmed before [35].

Additional information regarding the carrier separation and transport is provided by the EIS and C-V measurements. Figure 3c shows the Nyquist plots of the EIS measurements for the InGaN-4 NW array under illumination for varied light incidence angle between 0° and 80°, to investigate and confirm that increase of the angle of incidence enhances the light absorption and photoelectrochemical properties. The inset shows the corresponding equivalent circuit. The diameter of the half circle provides the charge transfer resistance R_{ct} which is related to the charge transfer of photogenerated carriers to the surface followed by the charge transfer through the InGaN/electrolyte interface [44]. R_{ct} continuously decreases with increase of the angle of incidence. As generally, R_{ct} decreases under illumination, that is, with photogenerated carrier generation, this agrees with the increased absorption for larger angles of light incidence. Therefore, the above result illustrates that increase of the angle of incidence enhances the light absorption, and then generates more photogenerated carriers, and finally reduces R_{ct}. To investigate the trapping effect of tilted nanowire arrays, we simulated the two-dimensional reflected electric field intensity distribution diagram of Si/InGaN nanowire structure via FDTD under the incident light with various angles in Figure 3d–f, corresponding to incident light of 0°, 50°, and 73° respectively, and the wavelength of incident polarized light is 550 nm. The detailed parameters can be seen in our previous work [35, 41]. The reflectance of Si/InGaN nanowires decreases from 0° to 50° to 73°, and the reflectance ratio is 1/0.63/0.39. Therefore, we can conclude that the tilted nanowire array structure has enhanced trapping effect than that of nanowire array parallel to the incident light. In addition, in the incident

light angle range of 0°–73°, with the increase of incident light angle, the trapping effect of nanowire array structure is stronger. The results are consistent with those in our previous work, that NW arrays on pyramidal (52° tilt angle) or oblique pyramidal (73° tilt angle) Si substrates can obvious enhance light adsorption compared with that on planar Si substrate [35, 41].

The dependence of the photocurrent density for the InGaN-1–4 photoanodes on the tilt angle of the incident light is studied in Figure 4a. The photocurrent is measured at a bias of 0.3 V versus Ag/AgCl and normalized to the projected illuminated geometrical surface area. The As the light incidence tilt angle increases, the photocurrent density for all the InGaN photoanodes undergoes a maximum which becomes larger in magnitude and shifts to larger tilt angles for the InGaN-1 to 4 photoanodes, which is consistent with the conclusions that the light response enhancement rate is proportional to the tilt angle within a certain range of tilt angle in Figure 3d. The maximum photocurrent density enhancement for InGaN-1 is 39% at the tilt angle of 63.1°. For the InGaN-2 and InGaN-3 photoanodes, the maximum photocurrent density enhancement is similar, of 55% at 72° and 54% at 73°, respectively. The maximum photocurrent density enhancement is largest for the InGaN-4 photoanode of 116% at the largest tilt angle of 81.9°. To provide an intuitive explanation for the photocurrent density enhancement, in Figure 4b,c, the geometrical arrangement for the optical light trapping and absorption mechanism is schematically drawn for dense and more separated NWs in the arrays. The blue colored regions indicate the light trapping depth. By simply assuming geometrical optics, multiple reflections and absorption accompanied with each reflection, it is directly evident that a maximum of absorption occurs at a certain tilt angle which both, the maximum of absorption and tilt angel, increase in magnitude with increasing NW separation. With increasing tilt angle the number of reflections increases while the light propagates deeper into the NW arrays for the same tilt angle for wider NW separation. For grazing light incidence angles, extensive accumulation of photo-generated holes close to the NW tops leads to screening of the near-surface electric field to reduce the carrier separation and transport [37]. Evidently, with respect to the tilt angle, the optical light trapping and absorption enhancements dominate for all NW arrays to govern the photocurrent density enhancement, also for InGaN-4. From the photocurrent performance in Figure 3b and Supporting Information: Figure S5, InGaN photoanodes with NW lengths of 268, 539, 854, and 833 nm show the photocurrent densities of 0.032, 0.039, 0.055, and 0.042 mA cm^{-2} at 0.3 V versus Ag/AgCl after 80 s, respectively. Regarding the NW length, the results in Figure 3b and Supporting Information: Figure S5 indicate that these lengths of four InGaN NWs have a relatively minor impact on photocurrent or light adsorption. This provides an estimate of the depth of the light trapping regions and implies that for the investigated longer NWs, length is not a parameter which is involved. As shown in Supporting Information: Table S1, our InGaN photoanode displays superior PEC performance in comparison of reported pure InGaN and GaN photoanodes, delivering photocurrent density of 65 μA cm^{-2} at a low potential of 0.3 V versus Ag/AgCl.

Figure 5a–d depicts the M-S plots of the C-V measurements for the InGaN-1–4 photoanodes in the dark to verify the carrier type and analyze the flat band voltage (V_{fb}) and near-surface energy band bending, according to [45, 46]:

$$\frac{1}{C_{sc}^2} = \frac{2}{A^2 \varepsilon_0 \varepsilon_r e N_d}\left(V_{app} - V_{fb} - \frac{k_B T}{e}\right) \quad (1)$$

where C_{sc}, A, ε_0, ε_r, N_d, V_{app}, and k_B are the capacitance of the space charge region, the photoelectrode area, vacuum permittivity, relative permittivity, ionized donor (or acceptor) concentration, applied bias (vs. reversible hydrogen electrode), and the Boltzmann constant. From the slope of the M-S plots, n-type conductivity is deduced. The unknown surface area does not

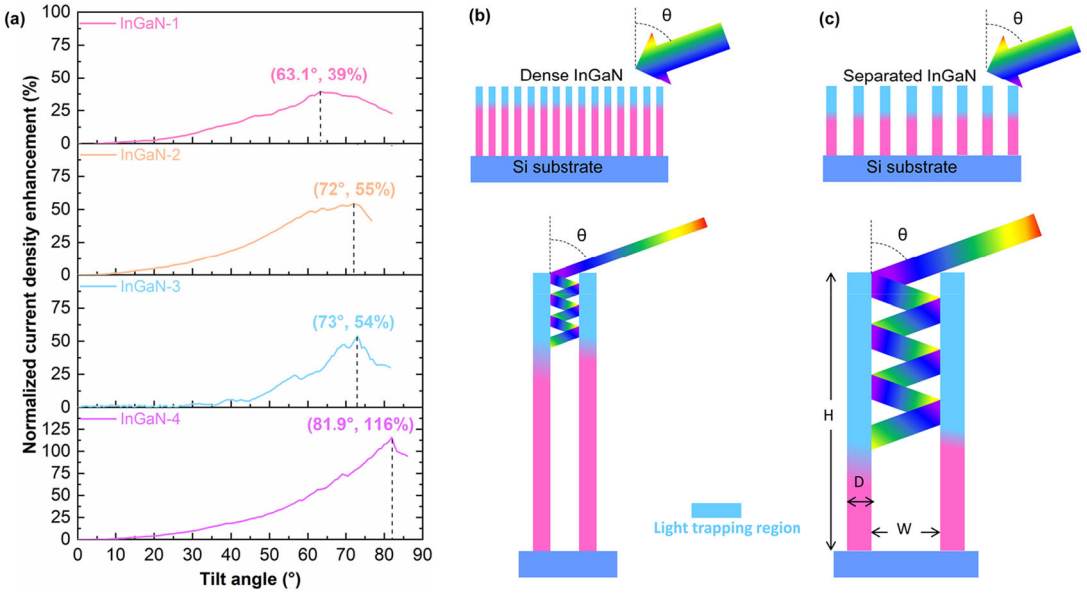

FIGURE 4 | (a) Normalized photocurrent density enhancement of InGaN-1, InGaN-2, InGaN-3, and InGaN-4 photoanodes at 0.3 V (vs. Ag/AgCl). Geometrical arrangement for the optical light trapping and absorption for (b) dense and (c) more separated nanowire (NW) arrays.

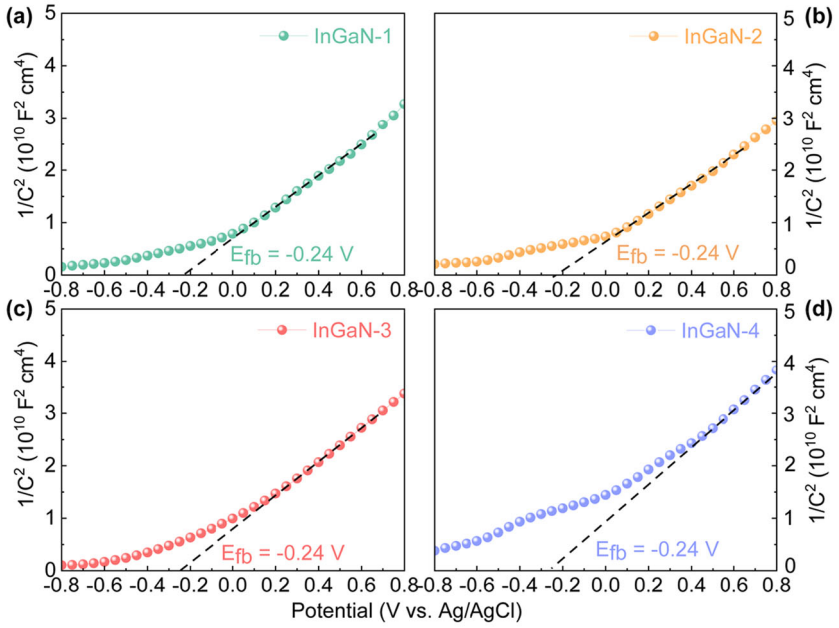

FIGURE 5 | Mott–Schottky (M-S) plots of the capacitance-voltage (C-V) measurements for (a) InGaN-1, (b) InGaN-2, (c) InGaN-3 and (d) InGaN-4 photoanodes in the dark.

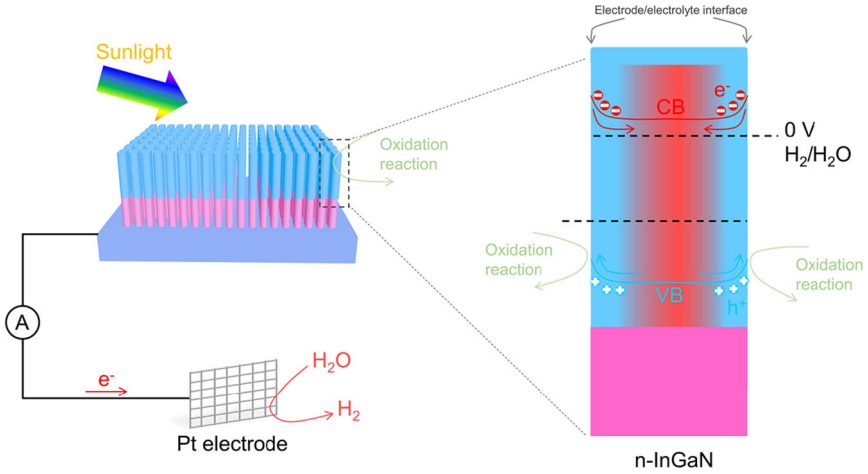

FIGURE 6 | Schematic illustration of the photoelectrochemical (PEC) system with energy band structure and photogenerated carrier transport for n-InGaN nanowire (NW) photoanodes.

allow the determination of the free electron concentrations. The V_{fb} values for the InGaN-1–4 photoanodes are all −0.24 V. The same value is expected from the same In content and corresponding same pinning of the surface Fermi level and indicates comparable carrier separation and transport in the near-surface electric field due to the upward near-surface energy band bending [47]. The band structure with photogenerated carrier separation and transport together with a schematic illustration of the whole PEC system and oxygen- and hydrogen evolution reactions is drawn in Figure 6 [48, 49].

4 | Conclusion

To conclude, we have designed and prepared InGaN NW arrays with the same In content but different morphologies using PA-MBE for PEC analysis. We have unraveled the relationship between the InGaN NW morphologies and light trapping as a function of the light angle of incidence for maximized solar light absorption and optimized PEC performance. For vertical light incidence, InGaN NW arrays with medium-density and well-separated NWs exhibited the maximum photocurrent due to enhanced light absorption combined with large surface area. For tilted light incidence the photocurrent for all studied InGaN NW arrays first increased, passed a maximum and then decreased with increasing angle of incident light. The InGaN NW arrays with more separated NWs exhibited the largest photocurrent enhancement of 116% for 81.9° light incidence angle. Furthermore, we also demonstrate from theoretical side of FDTD simulations tilt nanowires exhibit enhanced light adsorption. This study provides a systematic insight into the effects of various morphologies of InGaN NW arrays with different NW spacings, lengths and shapes on the PEC performance for varying angle of incident light. This is significant for the rational design of

hierarchical NW arrays on nonplanar substrates for maximized efficiencies photocatalytic and other optical devices.

Author Contributions

Guofu Zhou supervised the project. Wenhao Liang. and Hedong Chen conceived the idea for experiments. Hedong Chen, Mei Hu, and Yizhi Liao performed the material preparation experiments. Fan Xu, Dao Wang, Weiwei Feng, and Yecheng Qiu performed the performance test and material properties characterization. Hedong Chen, Wenhao Liang, and Yin Feng conducted data analysis. Hedong Chen, and Wenhao Liang wrote the manuscript. Fuming Chen, Wenhao Liang and Guofu Zhou polished the manuscript.

Acknowledgements

H. C., M. H. and Y. L. contributed equally to this study. This study was supported by the National Natural Science Foundation of China (12404049), Guangdong Basic and Applied Basic Research Foundation (2023A1515110521, 2024A1515011260), W. L. thanks for the financial support of Start-up Fund for RAPs under the Strategic Hiring Scheme (P0058663) in The Hong Kong Polytechnic University.

Conflicts of Interest

The authors declare no conflicts of interest.

References

1. Y. He, P. Tang, Z. Hu, et al., "Engineering Grain Boundaries at the 2D Limit for The Hydrogen Evolution Reaction," *Nature Communications* 11, no. 1 (2020): 1–12.

2. J. Di, J. Xiong, H. Li, and Z. Liu, "Ultrathin 2D Photocatalysts: Electronic-Structure Tailoring, Hybridization, and Applications," *Advanced Materials* 30, no. 1 (2018): 1–30.

3. G. Zhou, L. Xu, G. Hu, L. Mai, and Y. Cui, "Nanowires for Electrochemical Energy Storage," *Chemical Reviews* 119, no. 20 (2019): 11042–11109.

4. Y. Wang, H. Sun, Z. Yang, Y. Zhu, and Y. Xia, "Bismuth-Based Metal-Organic Frameworks and Derivatives for Photocatalytic Applications in Energy and Environment: Advances and Challenges," *Carbon Neutralization* 3, no. 4 (2024): 737–767.

5. T. Takata, J. Jiang, Y. Sakata, et al., "Photocatalytic Water Splitting With a Quantum Efficiency of Almost Unity," *Nature* 581, no. 7809 (2020): 411–414.

6. L. Wang, W. Lian, B. Liu, et al., "A Transparent, High-Performance, and Stable Sb_2S_3 Photoanode Enabled by Heterojunction Engineering With Conjugated Polycarbazole Frameworks for Unbiased Photoelectrochemical Overall Water Splitting Devices," *Advanced Materials* 34, no. 29 (2022): 1–9.

7. J. Kosco, M. Bidwell, H. Cha, et al., "Enhanced Photocatalytic Hydrogen Evolution From Organic Semiconductor Heterojunction Nanoparticles," *Nature Materials* 19, no. 5 (2020): 559–565.

8. A. Fujishima and K. Honda, "Electrochemical Photolysis of Water at a Semiconductor Electrode," *Nature* 238, no. 5358 (1972): 37–38.

9. P. Li, X. Yuan, M. Feng, F. Ran, D. Zhang, and S. Chen, "Fabrication of Tio_X/Sb_2Se_3/P-Nio_X Photocathode for Efficient Photoelectrochemical Water Reduction," *Applied Physics Letters* 119, no. 10 (2021): 1–7.

10. H. Wu, H. L. Tan, C. Y. Toe, et al., "Photocatalytic and Photoelectrochemical Systems: Similarities and Differences," *Advanced Materials* 32, no. 18 (2019): 1–21.

11. P. Zhang and X. W. Lou, "Design of Heterostructured Hollow Photocatalysts for Solar-To-Chemical Energy Conversion," *Advanced Materials* 31, no. 29 (2019): 1–18.

12. S. Tang, W. Qiu, S. Xiao, Y. Tong, and S. Yang, "Harnessing Hierarchical Architectures to Trap Light for Efficient Photoelectrochemical Cells," *Energy & Environmental Science* 13, no. 3 (2020): 660–684.

13. Y. Wei, J. Wan, N. Yang, et al., "Efficient Sequential Harvesting of Solar Light by Heterogeneous Hollow Shells With Hierarchical Pores," *National Science Review* 7, no. 11 (2020): 1638–1646.

14. S. Masudy-Panah, R. Katal, N. D. Khiavi, E. Shekarian, J. Hu, and X. Gong, "A High-Performance Cupric Oxide Photocatalyst With Palladium Light Trapping Nanostructures and a Hole Transporting Layer for Photoelectrochemical Hydrogen Evolution," *Journal of Materials Chemistry A* 7, no. 39 (2019): 22332–22345.

15. T. Kimura, S. Sato, K. Kataoka, T. Morikawa, and D. Nakamura, "Self-Assembled Single-Crystalline Gan Having a Bimodal Meso/Macropore Structure to Enhance Photoabsorption and Photocatalytic Reactions," *ACS Applied Materials & Interfaces* 11, no. 4 (2019): 4233–4241.

16. C. Yang, X. Xi, Z. Yu, et al., "Light Modulation and Water Splitting Enhancement Using a Composite Porous GaN Structure," *ACS Applied Materials & Interfaces* 10, no. 6 (2018): 5492–5497.

17. K. Choi, K. Kim, I. K. Moon, J. Bang, and J. Oh, "Subwavelength Photocathodesviametal-Assisted Chemical Etching of Gaas for Solar Hydrogen Generation," *Nanoscale* 11, no. 32 (2019): 15367–15373.

18. I. Oh, J. Kye, and S. Hwang, "Enhanced Photoelectrochemical Hydrogen Production From Silicon Nanowire Array Photocathode," *Nano Letters* 12, no. 1 (2011): 298–302.

19. K. Oh, V. Dorcet, B. Fabre, and G. Loget, "Dissociating Water at N-Si Photoanodes Partially Covered With Fe Catalysts," *Advanced Energy Materials* 10, no. 3 (2019): 1–8.

20. R. Fan, G. Huang, Y. Wang, Z. Mi, and M. Shen, "Efficient N^+P-Si Photocathodes for Solar H_2 Production Catalyzed by Co-W-S and Stabilized by Ti Buffer Layer," *Applied Catalysis, B: Environmental* 237 (2018): 158–165.

21. B. Tu, Y. Weng, F. Zheng, X. Su, L. Fang, and L. You, "Efficient Hydrothermal Growth of High-Performance MoS_2/Pyramid-Si Photocathodes by Surface Hydrophilicity Engineering," *Applied Physics Letters* 118, no. 15 (2021): 1–5.

22. Y. Zhao, W. Song, D. Wang, H. Chen, and G. Zhou, "Enhanced Light Trapping and Charge Separation via Pyramidal Cu_2O/NiCo-LDH Photocathode for Efficient Water Splitting," *ACS Applied Energy Materials* 5, no. 1 (2022): 992–1001.

23. J. Liu, Z. Luo, X. Mao, et al., "Recent Advances in Self-Supported Semiconductor Heterojunction Nanoarrays as Efficient Photoanodes for Photoelectrochemical Water Splitting," *Small* 18, no. 48 (2022): 1–26.

24. K. Ren, J. Zhou, Z. Wu, Q. Sun, and L. Qi, "Dual Heterojunctions and Nanobowl Morphology Engineered $BiVO_4$ Photoanodes for Enhanced Solar Water Splitting," *Small (Weinheim an der Bergstrasse, Germany)* 20, no. 1 (2024): 2304835.

25. T. Dursap, M. Fadel, P. Regreny, et al., "Enhanced Light Trapping In GaAs/TiO_2-Based Photocathodes for Hydrogen Production," *ACS Applied Materials & Interfaces* 15, no. 46 (2023): 53446–53454.

26. Z. Hu, H. Wu, S. Li, C. Zhang, R. Liang, and M. Zhou, "Solar-Driven Chloride Activation via 3D Oxygen-Vacancy-Rich TiO_2 Network Photoanode for Ultrafast and Durable Purification of Saline Wastewater," *Chemical Engineering Journal* 498 (2024): 155308.

27. X. Li, S. Xie, D. Hou, W. Wang, and G. Li, "Functionalized UIO-66 Induces Shallow Electron Traps in Heterojunctions With Inn for Enhanced Photocathodic Water Splitting," *Journal of Colloid and Interface Science* 685 (2025): 573–583.

28. Z. Hao, X. Sun, L. Zhang, et al., "Enhanced Recycling and Utilization of Industrial Waste Gas H_2S Through Photoelectrochemical Methods With $ZnFe_2O_4/ZnIn_2S_4$ Heterojunction Containing NiCoP Co-Catalyst," *Chemical Engineering Journal* 517 (2025): 164553.

29. M. Arif, H. Yang, Y. Jiang, et al., "Construction of Three-Dimensional $NiCo_2S_4$@Cu_2O Nanowires With a High Surface Photovoltage to Promote the Energy Efficiency of Photo-Assisted Supercapacitors," *Journal of Colloid and Interface Science* 698 (2025): 138067.

30. A. Standing, S. Assali, L. Gao, et al., "Efficient Water Reduction With Gallium Phosphide Nanowires," *Nature Communications* 6, no. 1 (2015): 7824.

31. Z. Xu, S. Zhang, F. Gao, L. Wen, Y. Yu, and G. Li, "Correlations Among Morphology, Composition, and Photoelectrochemical Water Splitting Properties of InGaN Nanorods Grown by Molecular Beam Epitaxy," *Nanotechnology* 29, no. 47 (2018): 475603.

32. J. Kamimura, P. Bogdanoff, J. Lähnemann, et al., "Photoelectrochemical Properties of (In,Ga)N Nanowires for Water Splitting Investigated by In Situ Electrochemical Mass Spectroscopy," *Journal of the American Chemical Society* 135, no. 28 (2013): 10242–10245.

33. W. J. Dong, Z. Ye, S. Tang, et al., "Concentrated Solar Light Photoelectrochemical Water Splitting for Stable and High-Yield Hydrogen Production," *Advanced Science* 11, no. 26 (2024): 1–9.

34. Y. Wei, L. Ke, J. Kong, et al., "Enhanced Photoelectrochemical Water-Splitting Effect With a Bent ZnO Nanorod Photoanode Decorated With Ag Nanoparticles," *Nanotechnology* 23, no. 23 (2012): 235401.

35. H. Chen, P. Wang, H. Ye, et al., "Vertically Aligned InGaN Nanowire Arrays on Pyramid Textured Si (1 0 0): A 3D Arrayed Light Trapping Structure for Photoelectrocatalytic Water Splitting," *Chemical Engineering Journal* 406 (2021): 126757.

36. Y. Wang, Y. Wu, K. Sun, and Z. Mi, "A Quadruple-Band Metal–Nitride Nanowire Artificial Photosynthesis System for High Efficiency Photocatalytic Overall Solar Water Splitting," *Materials Horizons* 6, no. 7 (2019): 1454–1462.

37. J. Wu, Y. Li, J. Kubota, et al., "Wafer-Scale Fabrication of Self-Catalyzed 1.7 ev GaAsP Core–Shell Nanowire Photocathode on Silicon Substrates," *Nano Letters* 14, no. 4 (2014): 2013–2018.

38. P. Wang, H. Chen, H. Wang, et al., "Multi-Wavelength Light Emission From InGaN Nanowires on Pyramid-Textured Si(100) Substrate Grown by Stationary Plasma-Assisted Molecular Beam Epitaxy," *Nanoscale* 12, no. 16 (2020): 8836–8846.

39. J. Xie, Ü. Özgür, Y. Fu, et al., "Low Dislocation Densities and Long Carrier Lifetimes in GaN Thin Films Grown on a Sin_x Nanonetwork," *Applied Physics Letters* 90, no. 4 (2007): 2433754.

40. D. Zhu, C. McAleese, M. Häberlen, et al., "High-Efficiency InGaN/GaN Quantum Well Structures on Large Area Silicon Substrates," *physica status solidi (a)* 209, no. 1 (2011): 13–16.

41. H. Chen, P. Wang, X. Wang, et al., "3D InGaN Nanowire Arrays on Oblique Pyramid-Textured Si (311) for Light Trapping and Solar Water Splitting Enhancement," *Nano Energy* 83 (2021): 105768.

42. H. Zhang, M. Ebaid, J.-W. Min, T. K. Ng, and B. S. Ooi, "Enhanced Photoelectrochemical Performance of InGaN-Based Nanowire Photoanodes by Optimizing the Ionized Dopant Concentration," *Journal of Applied Physics* 124, no. 8 (2018): 1–8.

43. M. Ebaid, J.-W. Min, C. Zhao, T. K. Ng, H. Idriss, and B. S. Ooi, "Water Splitting to Hydrogen over Epitaxially Grown InGaN Nanowires on a Metallic Titanium/Silicon Template: Reduced Interfacial Transfer Resistance and Improved Stability to Hydrogen," *Journal of Materials Chemistry A* 6, no. 16 (2018): 6922–6930.

44. R. Zhang, B. Zhang, J. Lv, et al., "Heteropore Conjugated Organic Reticular Subnano-Crystal for Photocatalytic Water Splitting," *Carbon Neutralization* 4, no. 3 (2025): 1–11.

45. P. Varadhan, H.-C. Fu, D. Priante, et al., "Surface Passivation of GaN Nanowires for Enhanced Photoelectrochemical Water-Splitting," *Nano Letters* 17, no. 3 (2017): 1520–1528.

46. B. Zhai, J. He, H. Li, et al., "Integral Morphology and Structure Design of Poly (Heptazine Imide) for Efficient Utilization of Visible Light Generated Charge Carriers in Proton Reduction Reactions," *Carbon Neutralization* 3, no. 5 (2024): 888–903.

47. J. Lin, Y. Yu, Z. Zhang, et al., "A Novel Approach for Achieving High-Efficiency Photoelectrochemical Water Oxidation in InGaN Nanorods Grown on Si System: Mxene Nanosheets as Multifunctional Interfacial Modifier," *Advanced Functional Materials* 30, no. 13 (2020): 1–11.

48. R. T. Elafandy, M. Ebaid, J.-W. Min, C. Zhao, T. K. Ng, and B. S. Ooi, "Flexible InGaN Nanowire Membranes for Enhanced Solar Water Splitting," *Optics Express* 26, no. 14 (2018): A640–A650.

49. J. Kamimura, P. Bogdanoff, P. Corfdir, O. Brandt, H. Riechert, and L. Geelhaar, "Broad-Band Light Absorption and High Photocurrent of (In,Ga)N Nanowire Photoanodes Resulting From a Radial Stark Effect," *ACS Applied Materials & Interfaces* 8, no. 50 (2016): 34490–34496.

Supporting Information

Additional supporting information can be found online in the Supporting Information section.
Supporting Information Hioki.